# DARK MATTER CONSTRAINTS AND THE NEUTRALINO SECTOR OF THE SCNMSSM

#### A PREPRINT

## Elham Aldufeery\*

Department of Physics and Astronomy, Female Campus King Saud University Riyadh, Saudi Arabia 437203161@student.ksu.edu.sa

#### Maien Y. Binjonaid

Department of Physics and Astronomy King Saud University Riyadh, Saudi Arabia maien@ksu.edu.sa

July 5, 2022

#### **ABSTRACT**

The neutralino sector of the semi-constrained next-to-minimal supersymmetric standard model is explored under recent experimental constraints, with special attention to Dark Matter limits. The effects of Dark Matter relic density upper and lower bounds, and recent direct detection constraints on spin-dependent and independent cross-sections (proton and neutron), are thoroughly analyzed. Particularly, we show which regions of the parameter space are ruled-out due to the different Dark Matter constraints and the corresponding model-specific parameters:  $\lambda, \kappa, A_{\lambda}$  and  $A_{\kappa}$ . Additionally, we analyze all annihilation and co-annihilation processes (with heavier neutralinos and charginos) that contribute to the dark matter relic density. The mass components of the dark matter candidate, the lightest neutralino  $\tilde{\chi}^0_1$ , are studied, and the decays of heavy neutralinos and charginos, especially  $\tilde{\chi}^0_2$  and  $\tilde{\chi}^+_1$ , into the lightest neutralino are probed. We impose semi-universal boundary conditions at the GUT scale, and require a moderate range of  $\tan\beta\lesssim 10$ . We find that the allowed parameter space is associated with a heavy mass spectrum in general, and that the lightest neutralino is mostly Higgsino with a mass range that resides mostly between 1000 GeV and 1500 GeV.

Keywords NMSSM · Dark Matter

## 1 Introduction

The nature of Dark Matter (DM) continues to be a mystery, even though there is an abundance of evidence for its existence [1–6]. A well-motivated candidate for DM is the neutralino LSP in SUSY models [7]. However, such models are being challenged by recent null results from experiments, including DM searches [8–13]. The latter can be categorized into collider, direct detection, and indirect detection searches. Collider searchers rely on detecting missing energy events that could arise from decays into DM particles, indirect detection depends on observations of astronomical events, such as gamma ray lines, and direct detection searches rely on observing possible elastic scattering events between DM particles and atomic nuclei (a comprehensive review is given in [14]). One of the most considered low-scale SUSY models is the NMSSM (reviewed in [15,16]), which opens new possibilities given that its neutralino sector is richer than that in the MSSM. A fact that is attributed to the inclusion of a SM-Singlet superfield, which is absent in the MSSM. The inclusion of such a singlet is motivated by explaining the origin of the  $\mu$ -term in the MSSM and increasing the predicted SM Higgs mass at tree-level.

The issue of DM in the NMSSM has been and still is the center of attention of researchers in the field [17–31]. The case of low-mass neutralino LSP has been investigated with attention to the interesting cases large singlino-higgsino mixture, or singlino-like DM [23, 32–35]. Additionally, the implications of direct and indirect detection for the NMSSM and its extensions were detailed in [22, 36–42]. Most recently, the authors of [43] studied the NMSSM and DM, where low-scale input parameters were used, and the attention is targeted towards future searches. However, most of these

<sup>\*</sup>Alternative email: elham.dufeery@gmail.com

works do not include the most recent constraints from DM searches, especially those coming from direct detection. Moreover, from a phenomenology point of view, it is interesting to understand in-details how current limits affect the NMSSM with the well-motivated GUT boundary conditions, in terms of the affected regions of the parameters, and more physically, which channels contribute to DM relic density, the branching ratio of chargino/neutralino to the LSP.

Considering all this, we explore, exploiting state-of-art tools incorporating latest DM constraints, the parameter space of the NMSSM under semi-constrained boundary conditions at the GUT scale, given that a major motivation for SUSY models is to provide gauge coupling unification. Particularly, we analyze how relic density abundance constraints, as well as recent direct detection limits affect the model, without particular focus on specific regions except for relatively moderate  $\tan \beta \lesssim 10$ , which motivated by enhancing the tree-level prediction of the SM-like Higgs mass in the model. We present the portions of the parameter space that pass all known constraints (apart from g-2 of the muon), and show those regions which fail the aforementioned DM constraints, providing a deeper insight into the model that usually overlooked in recent literature.

The paper is organized as follows. In Section 2, a brief overview of the superpotential of the NMSSM and the neutralino mass matrix is provided, and this is where the necessary parameters of the model are introduced. Next, Section 3 specifies the boundary conditions of model, and presents our methodology of probing the parameter space of the model, and the relevant non-DM and DM constraints taken into account. In Section 4, the results are presented and divided into subsections corresponding to the various aspects of the neutralino section that are considered as mentioned earlier. Section 5 is where we discuss the results, comparing them to recent literature, and conclude the paper.

#### 2 The NMSSM and its Neutralino Sector

The NMSSM is characterized by the following superpotential,

$$\mathcal{W} = \mathcal{W}_{\text{MSSM}}^{\not l} + \lambda \hat{S} \hat{H}_u \cdot \hat{H}_d + \frac{1}{3} \kappa \hat{S}^3, \tag{1}$$

where  $\mathcal{W}_{\text{MSSM}}^{\not l}$  encodes the Yukawa couplings as in the MSSM. The second term replaces the  $\mu$ -term in the MSSM so that it is dynamically generated when the singlet superfield  $\hat{S}$  acquires a vacuum expectation value (VEV).  $\lambda$  is the coupling between  $\hat{S}$  and the up and down Higgs superfields  $\hat{H}_u$ ,  $\hat{H}_d$ . The third term represents the cubic self-coupling of  $\hat{S}$ . This  $\kappa$  term is included to maintain a  $\mathbb{Z}_3$  invariance in the model.

In contrast to the MSSM, the soft-SUSY breaking lagrangian of the NMSSM contains extra terms associated with trilinears terms  $A_{\lambda}$  and  $A_{\kappa}$ , as well as a soft-SUSY breaking mass term for the singlet. The Higgs sector of the model receives extra contributions from the singlet, and the number of Higgs bosons is increased to seven particles (two charged, 3 CP-even, and 2 CP-odd). Furthermore, the neutralino sector is also affected by the presence of the new NMSSM-specific terms. As opposed to the  $4\times 4$  mass matrix in the MSSM, the neutralino mass matrix in the NMSSM is  $5\times 5$ , which reads,

$$\mathcal{M}_{0} = \begin{pmatrix} M_{1} & 0 & -\frac{g_{1}v_{d}}{\sqrt{2}} & \frac{g_{1}v_{u}}{\sqrt{2}} & 0\\ & M_{2} & \frac{g_{2}v_{d}}{\sqrt{2}} & -\frac{g_{2}v_{u}}{\sqrt{2}} & 0\\ & & 0 & -\mu & -\lambda v_{u}\\ & & & 0 & -\lambda v_{d}\\ & & & & 2\kappa s \end{pmatrix},$$
(2)

where  $M_{1,2}$  represent gaugino masses, while  $\mu=\lambda s$  is the effective mu-term.  $g_{1,2}$  denote gauge couplings,  $v_{u,d},s$  indicate VEVs of the up- and down-Higgs fields, and singlet field. The rest of parameters were defined previously. Upon diagonalization, the mass eigenstates are ordered from small to large as  $\tilde{\chi}^0_1,\ldots,\tilde{\chi}^0_5$ , where the first is the lightest neutralino, which is usually the LSP of the model and the dark matter candidate.

Finally, the NMSSM can be specified at the GUT scale by a number of input parameters, which are: a soft-SUSY breaking scalar mass parameter  $(m_0)$ , a soft-SUSY breaking gaugino mass parameter  $(m_{1/2}$ , a soft-SUSY breaking trilinear parameter  $A_0$ , the ratio between the VEVs of up- and down- Higgs fields  $\tan \beta = v_u/v_d$ , an effective Higgs/Higgsino mass parameter  $\mu_{\rm eff} = \lambda s$ , a singlet-doublet coupling parameter  $\lambda$ , and a singlet coupling parameter  $\kappa$ . It is desirable to understand how NMSSM-specific parameters behave and affect the model's predictions, and therefore, it is often the case that one treats the two trilinear soft-SUSY breaking parameters  $A_{\lambda}$  and  $A_{\kappa}$  differently from  $A_0$ .

## 3 The parameter space

NMSSMTools (v5.5.2) was used to generate the mass spectrum of the model. NMSSMTools utilizes MicrOmega<sup>2</sup>, which in turn, calculates the relevant DM observables of the model. All theoretical and experimental constraints where taken into account apart from the  $(g-2)_{\mu}$  anomaly. These constraints include limits on the decays of both the K and B mesons, on the SM Higgs mass, couplings, and decays (including exotic decays), on supersymmetric particles. Theoretical constraints include reaching a global minimum, no negative physical mass values, successful EWSB in the Higgs sector.

Moreover, the package was modified to our purpose, which is to analyze each DM constraint separately (after imposing non-DM constraints). This enable us to understand and report on how DM limits affects the considered model. However, and as far as DM constraints are concerned, in this paper, we have restricted our analysis to constraints on DM relic density and direct detection.

With this in mind, we explore the parameter space focusing on specific regions where  $\tan \beta \lesssim 10$ , but allow  $\lambda$  to vary as shown in Table 1. We specify the inputs of the model at the GUT scale in what is commonly called the scNMSSM as explained in the previous Section. The ranges of the input parameters are shown in Table 1.

Parameter	Range		
$m_0$	[500-5000]GeV		
$m_{1/2}$	[500-5000]GeV		
$A_0, A_{\lambda}, A_{\kappa}$	[-3000-3000]GeV		
$\mu_{ m eff}$	[100-1500]GeV		
$\tan \beta$	[1-10]		
$\lambda, \kappa$	[0.1-0.7]		
Table 1			

It is important to note that the ranges for the trilinear parameters are varied separately, and the same is true for  $\lambda$  and  $\kappa$ . The latter parameters are specified in the low-scale, and  $m_{h_i}^2$  (i=u,d) is calculated by NMSSMTools at the GUT-scale given the specified input parameters (for more details about how NMSSMTools computes the spectrum we refer the reader to the relevant literature [44–48]).

Finally, it is worth mentioning that the latest version of NMSSMTools utilizes MicrOMEGAsv5.0, and includes a number of recent and important constraints on Higgs physics [49–51], as well as DM limits on spin independent cross-sections from DarkSide-50 [52] and CRESST-II [53], and limits on spin dependent cross-sections from XENON1T [54] and PICO60 [55].

## 4 Numerical Results

## 4.1 Mappiong DM constraints into the models' parameters

Figures 1, 2, and 3 show the results in the  $(A_{\lambda}-A_{\kappa})$ ,  $(\lambda-\kappa)$ , and  $(m_0-m_{1/2})$  planes, respectively. Each Figure contains a number of sub-figures that represent the allowed points in green and the ruled-out points in red. Each sub-figure also represents one type of problem causing the red points to be ruled-out.

In Fig. 1, it can be seen in the top-left panel that the ruled-out points are associated with no DM candidate in the model. Basically, this reflects results where the LSP is a charged particle (hence cannot be a DM candidate), or that the input parameters did not lead to successful solutions causing the algorithm of MicrOMEGAs to stop. This issue becomes more relevant as both  $A_{\lambda}$  and  $A_{\kappa}$  increase, especially for  $A_{\lambda} > -2000$  GeV. On the other hand, the top-right panel shows the ruled-out points which predict too large values of the relic density  $\Omega h^2 \gtrsim 0.131$ , while the middle-left panel shows red points with  $\Omega h^2 \lesssim 0.107$ . Comparing the two plots indicates that in the scanned parameter space, most the problematic points (passing all non-DM constraints still) are associated with too small values for DM relic density<sup>3</sup>. As for cross-sections, the middle-left panel presents models predicting a DM direct detection rate that is too large (spin-independent cross-section)  $\sigma_{SI}^p > 7.30984120 \times 10^{-10}$  pb, which resembles the density of ruled-out points due to  $\Omega h^2$  being too small in the previously described plot. This shows that both of these limits play a major effect in constraining the scNMSSM, and it warns against common practice of imposing the upper limit on  $\Omega h^2$  only,

<sup>&</sup>lt;sup>2</sup>The interfacing is done by the authors of NMSSMTools.

<sup>&</sup>lt;sup>3</sup>Such models might be accepted if DM is not provided by the LSP of the NMSSM. However, other DM constraints should be taken into account to accord with observations.

since even if one accepts a point with too small relic density, such a point might be ruled-out by direct detection constraints. Next, the ruled-out points due to spin-dependent cross-sections,  $\sigma_{SD}^n > 1.19254077 \times 10^{-4}$  pb and  $\sigma_{SD}^p > 2.87997774 \times 10^{-4}$  pb, are shown in the bottom-left panel and bottom-right panel, respectively. Clearly, such constraints have smaller impact, but can eliminate parts of the model where both  $A_{\lambda}$  and  $A_{\kappa}$  are positive. In all the previous sub-figures, it is clear that DM constraints heavily affect regions where both trilinears are positive and large. Lastly, and focusing on the allowed points (shown in green), the Figure shows that when  $A_{\lambda} < 0$ , only negative  $A_{\kappa}$  can lead to successful predictions. However, as  $A_{\lambda}$  becomes positive,  $A_{\kappa}$  can take positive values.

To facilitate comparison and acquire a deeper insight, the same results are presented in the  $\lambda$ - $\kappa$  plane, as is shown in Fig. 2. Some of the data passing all non-DM restrictions still failed to produce a successful DM candidate (top-left panel), this took place particularly in the region  $0.4 < \lambda < 0.7$  and  $0.3 < \kappa < 0.6$ . Other points failed to comply with the upper limit on  $\Omega h^2$  (top-right panel), which occurs in all of the parameter space, but as clearly shown, regions where  $\lambda \gtrsim 0.55$  with  $\kappa \lesssim 0.2$  suffer from this problem as no allowed points can be found there (given our choices of inputs). The middle-left panel shows the case where  $\Omega h^2$  is too small. Comparing this result with that of too large  $\sigma_{SI}^p$ , it is clear that these two problems have the main impact as stated before. This impact is reflected in the  $\lambda$ - $\kappa$  plane for large values of  $\lambda$  accompanied with small values of  $\kappa$ . In the same region, we can see in both the bottom-left, and -right panels that the limits of spin-dependent cross-sections affect the same "bad" region.

Finally, Fig. 3 shows the results in the common  $(m_0$ - $m_{1/2})$  plane, which in turn provides further understanding of the how DM constraints impact the parameter space of the model, and enables comparison with other low-scale SUSY models such as the MSSM. As can be seen in the top-left panel, the issue of not obtaining a successful DM candidate is concentrated in regions where  $m_0 \lesssim 1200$  GeV. On the other hand, most of the ruled-out points due to predicting large  $\Omega h^2$  are associated with  $m_{1/2} < 3000$  GeV (top-right panel). Moreover, the two main problems causing the ruling-out of the red points, that is small  $\Omega h^2$  and large  $\sigma_{SI}^p$ , are common in the whole parameter space (see middle panels), whereas the limits on the spin-dependent cross-sections are mainly present in the region where  $m_{1/2} < 3000$  GeV. However, these are somewhat less relevant than the previous two constraints which occur in the same area. These results also show that the good points (in green) are concentrated in regions where  $m_{1/2} > 3000$  GeV. Such a large value for  $m_{1/2}$ , which in turn is needed to satisfy other non-DM limits, indicates a heavy mass spectrum, which is certainly the case in the studied parameter space.

#### 4.2 Properties of the mass of the neutralino DM

Now that we have an understanding of how recent DM constraints affects the parameters of the model. It is crucial to analyze the DM particle in terms of its mass content. In the allowed parameter space, the LSP represents a valid DM candidate, and has a mass range that is mostly concentrated between 1000 GeV and 1200 GeV. Lighter and heavier values still exist in our results, but such cases are sparse.

Fig. 4 shows the LSP mass components as a function of LSP mass. The top-left panel represents the Higgsino component, where the points split into two regions, with large and small contributions to the LSP mass. The region with higher contribution occurs in the range  $916 \le m_{\tilde{\chi}_1^0} \le 1526$  GeV with a maximum contribution of  $\sim 0.7$ . However, most of the data lie between  $1026 \le m_{\tilde{\chi}_1^0} \le 1396$  GeV. The lowest contribution in this region is 0.68 at  $m_{\tilde{\chi}_1^0} \approx 1200$  GeV. On the other hand, the concentration of data points decreases as  $m_{\tilde{\chi}_1^0} > 1396$  GeV. Meanwhile, the region with very small Higgsino component occurs in the range  $313 \le m_{\tilde{\chi}_1^0} \le 1294$  GeV, with a maximum contribution of 0.27 at  $m_{\tilde{\chi}_1^0} \approx 912$  GeV and the minimum contribution is about 0.036 at  $m_{\tilde{\chi}_1^0} \approx 452$  GeV.

In addition, the Singlino component as a function of LSP mass shown in the top-right panel. Again, the data points split into two regions with high and low Singlino contribution to the LSP mass. The region with higher contribution occurs between  $313 \le m_{\tilde{\chi}_1^0} \le 1149$  GeV. The contribution corresponding to the lower mass is about 0.98, while that associated with the higher mass is roughly 0.97. The maximum Singlino contribution is found to be approximately equal to 0.99 at  $m_{\tilde{\chi}_1^0} \approx 1106$  GeV. In contrast, the minimum contribution is found to be roughly 0.92 at  $m_{\tilde{\chi}_1^0} \approx 912$  GeV. Meanwhile, the region with a lower Singlino contribution occurs between  $691 \le m_{\tilde{\chi}_1^0} \le 1526$  GeV, where the Singlino component is found to be about 0.0026, and 0.022 for the lower and higher mass, respectively. The maximum contribution in this region is about 0.27 at  $m_{\tilde{\chi}_1^0} \approx 1200$  GeV. However, most of the data points lie between  $1025 \le m_{\tilde{\chi}_1^0} \le 1290$  GeV and cover a range of Singlino contributions between  $\sim 0.0002 - 0.06$ , which is a negligible contribution. Hence, the scanned parameter space, it is very difficult to find a Singlino-like DM candidate.

Furthermore, the bottom-left panel of Fig. 4 show that the Wino contribution to the LSP mass is always small in the explored parameter space. This region occurs at  $313 \le m_{\tilde{\chi}_1^0} \le 1525$  GeV, where the low and large mass are associated with Wino component of 0.004 and 0.03, respectively. However, the majority of data points lie between  $1030 \le m_{\tilde{\chi}_1^0} \le 1347$  GeV where the Wino contribution is in the range 0.02 - 0.05.

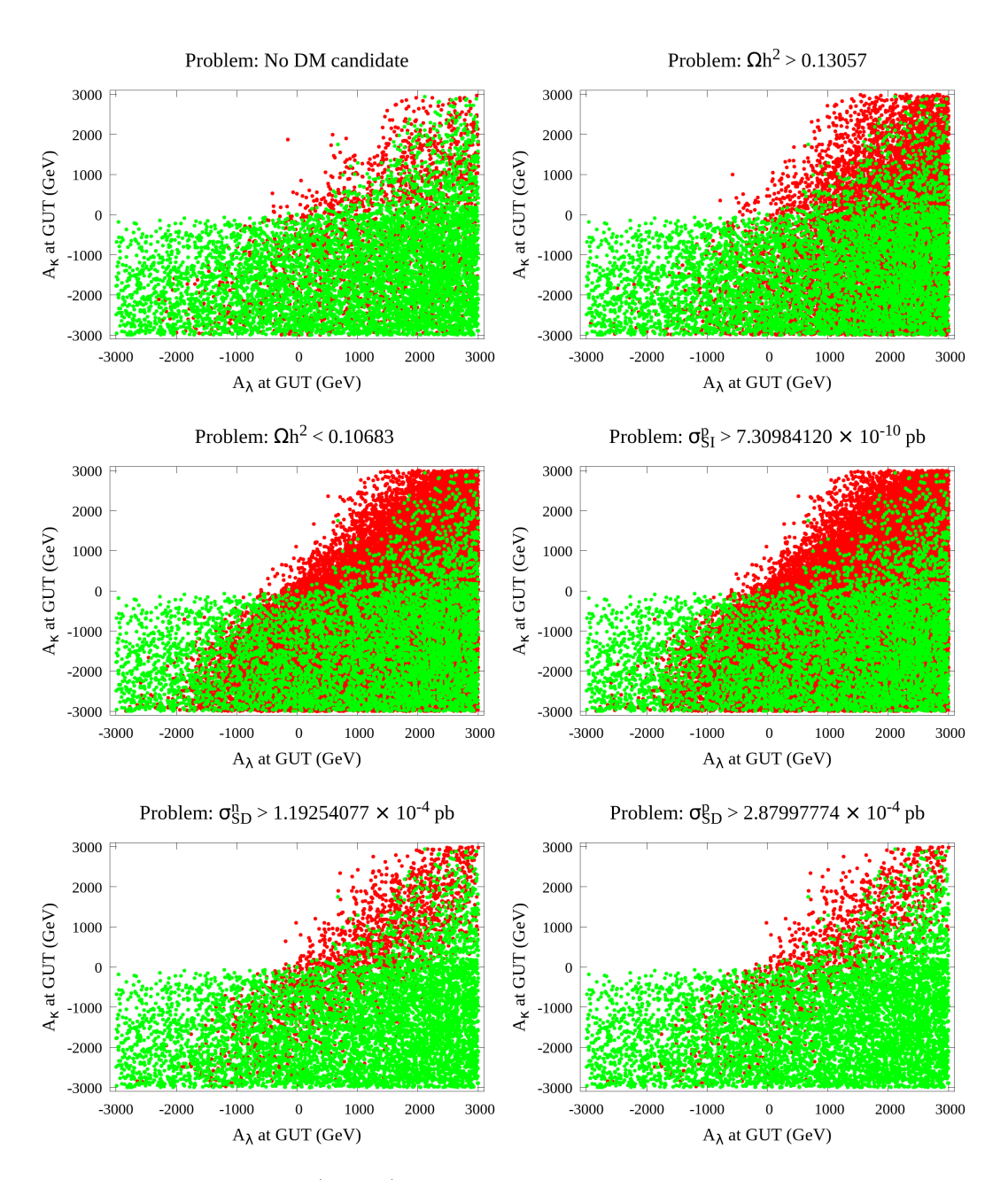


Figure 1: DM constraints in the  $(A_{\lambda}-A_{\kappa})$  plane. Red points are ruled-out, while green points are allowed.

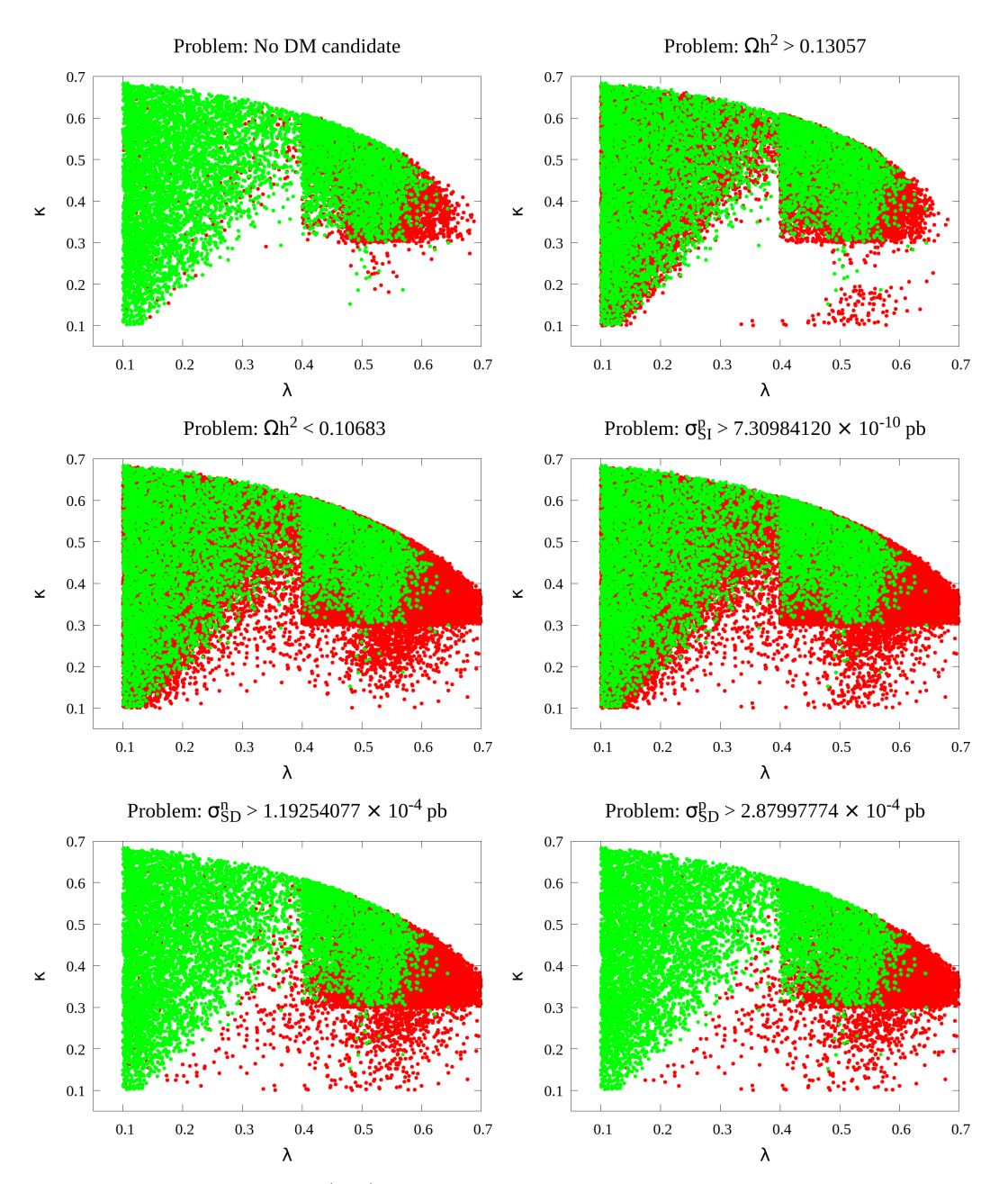


Figure 2: DM constraints in the  $(\lambda - \kappa)$  plane. Red points are ruled-out, while green points are allowed.

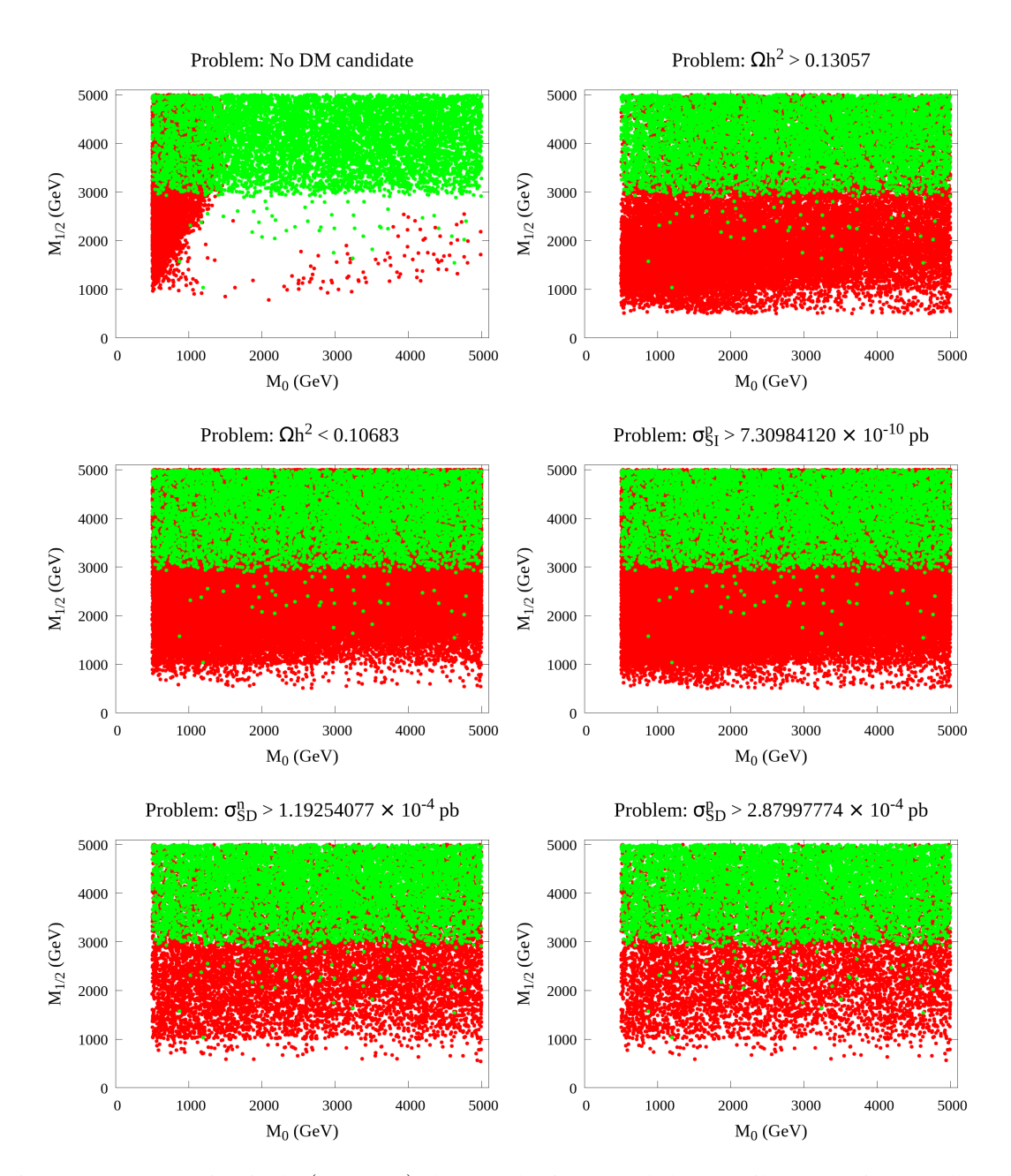


Figure 3: DM constraints in the  $(m_0$ - $m_{1/2})$  plane. Red points are ruled-out, while green points are allowed.

The Bino components are given in the bottom-right panel of Fig. 4, where it is clear that the data points split into two regions with higher and lower contribution to the LSP mass. The region with large Bino contribution occurs at  $451 \le m_{\tilde{\chi}_1^0} \le 1294$  GeV, where the value of the component is 0.99 (for the small end of the mass) and 0.98 (for the large end of the mass). The maximum Bino contribution is almost unity and occurs at  $m_{\tilde{\chi}_1^0} = 923$ , 1015 GeV. However, as can be seen in the Figure, most of the allowed points lie outside of this high Bino contribution region. Indeed, the region with low Bino contribution occurs at  $313 \le m_{\tilde{\chi}_1^0} \le 1526$  GeV, where the component takes the values 0.005, and 0.053, respectively. The maximum Bino contribution in this "low" region is about 0.2, which lies at  $m_{\tilde{\chi}_1^0} = 1431$  GeV. The area where the allowed data is concentrated is the mass range  $1032 \le m_{\tilde{\chi}_1^0} \le 1346$  GeV, where the Bino contribution assumes values roughly between 0.03-0.12.

Finally, the results above show that in the model under consideration, the LSP is mostly Higgsino. The bino and singlino components are small and somewhat comparable in most of the parameter space, expect very rarely where both can be close to unity (in such rare cases, the Higgsino component is very small). The wino component is always negligible.

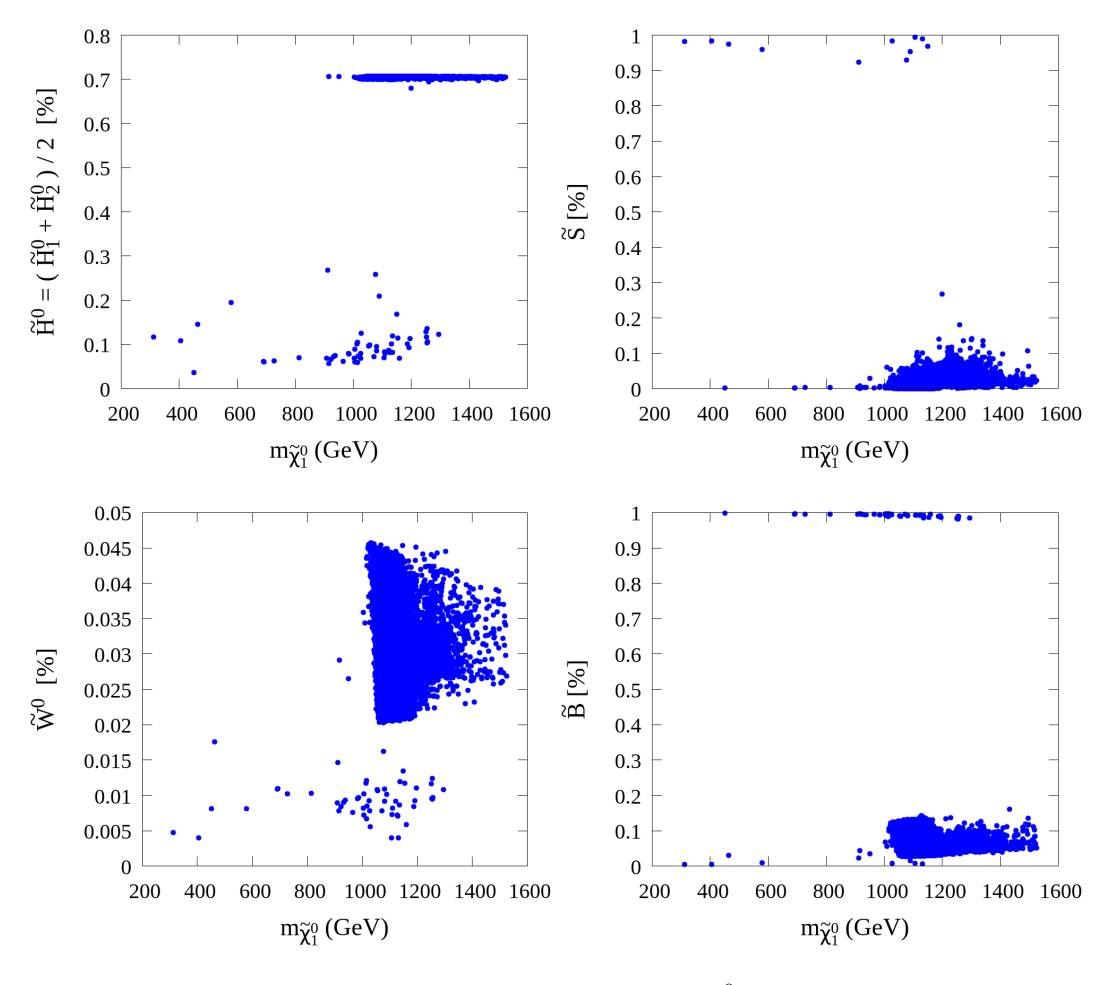


Figure 4: Mass components of  $\tilde{\chi}_1^0$ .

#### 4.3 Contributions to dark matter relic density

There are several annihilation and co-annihilation processes that contribute to the dark matter relic density. Here, we present the results for those processes that can contribute more than 1%. In the relevant plots, all of the points with zero y-axis correspond to data points that have a contribution of less than 1%. The exact values were not included in the output routine since these are very small (and hence there were set to zero in the plotting command), but those values are indeed taken into account in MicrOMEGAs and NMSSMTools for the calculation of the thermally averaged cross-section and the corresponding relic density.

Fig. 5 illustrates the contribution to DM relic density in percent for the annihilation and co-annihilation modes. The annihilation mode  $\tilde{\chi}_1^0 \tilde{\chi}_1^0 \to W^+ W^-$  is given in the top-left panel, where the data spread between  $m_{\tilde{\chi}_1^0} = 315$  GeV at the lower end, corresponding to a contribution of about 1%, and  $m_{\tilde{\chi}_1^0} = 1526$  GeV at the higher end, corresponding to a contribution of about 1.5%. Most of the data points cover a mass range of  $m_{\tilde{\chi}_1^0} = 1018 - 1350$  GeV with contribution of 1.72 - 3.66%. The largest contribution from this process is about 25%, corresponding to  $m_{\tilde{\chi}_1^0} = 1516$  GeV and the smallest contribution is about 1% corresponding to  $m_{\tilde{\chi}_1^0} = 315$  GeV.

In addition, the annihilation channel  $\tilde{\chi}_1^0 \tilde{\chi}_1^0 \to ZZ$  is show in the top-right panel. In this case the data points spread from a lower value of  $m_{\tilde{\chi}_1^0} = 693$  GeV, corresponding to a contribution of 1.1%, and a higher value of  $m_{\tilde{\chi}_1^0} = 1526$ , GeV corresponding to the contribution 1.24%. The maximum contribution is 13.2% which corresponds to  $m_{\tilde{\chi}_1^0} = 1514$  GeV, while the minimum contribution is 1.1% corresponding to  $m_{\tilde{\chi}_1^0} = 1487$  GeV. the majority of data points lie in the range  $m_{\tilde{\chi}_1^0} = 1028 - 1347$  GeV with contributions between 2.95 - 1.57%.

Meanwhile, the left panel in the second row shows the contribution to DM relic density for the annihilation mode  $\tilde{\chi}_1^0 \tilde{\chi}_1^0 \to t\bar{t}$ . In this case, the lower end of the mass starts at a value of  $m_{\tilde{\chi}_1^0} = 314$  GeV, corresponding to a contribution of 80%, while the higher mass value is  $m_{\tilde{\chi}_1^0} = 1522$  GeV, corresponding to the contribution 14%. The maximum contribution to the relic density is 99%, corresponding to an LSP mass of  $m_{\tilde{\chi}_1^0} = 1007$  GeV. Most of the data points set in the range  $m_{\tilde{\chi}_1^0} = 1161 - 1290$  GeV, with contributions in the range 5.75 - 0.69%, where 0.69% represents the minimum contribution.

In addition, the co-annihilation modes  $\tilde{\chi}_1^0 \tilde{\chi}_1^+ \to u \bar{d}, c \bar{s}$  are illustrated in the right panel of the second row, and the left panel of the third row, respectively. Here, the data points spread between a lower value of  $m_{\tilde{\chi}_1^0} = 913$  GeV, corresponding to the contribution 1.1%, and a higher value of  $m_{\tilde{\chi}_1^0} = 1528$  GeV, corresponding to the contribution 5%. The maximum contribution is 9.4% which corresponds to  $m_{\tilde{\chi}_1^0} = 1019$  GeV, the minimum contribution is 1.1% corresponding to  $m_{\tilde{\chi}_1^0} = 913$  GeV. Most of the allowed points are located in the range  $m_{\tilde{\chi}_1^0} = 1029 - 1330$  GeV, with a contribution range of 9-7%.

The co-annihilation mode  $\tilde{\chi}_1^0 \tilde{\chi}_1^+ \to tb$  is given in the right panel of the third row. The allowed points spread between a lower  $m_{\tilde{\chi}_1^0} = 580$ , GeV corresponding to the contributions 1.45%, and a higher value  $m_{\tilde{\chi}_1^0} = 1526$  GeV, corresponding to the contribution 3.46%. The maximum contribution is 8.36% which corresponds to  $m_{\tilde{\chi}_1^0} = 914$  GeV, while the minimum contribution is 1.01% corresponding to  $m_{\tilde{\chi}_1^0} = 1195$  GeV . Most of the data points are located at  $m_{\tilde{\chi}_1^0} = 1023 - 1400$  GeV with a contribution range 7.31 - 3.41%.

Furthermore, the bottom-left panel shows the co-annihilation channel  $\tilde{\chi}_1^0 \tilde{\chi}_1^+ \to H_2 W^+$ . In this case, the data points spread between  $m_{\tilde{\chi}_1^0} = 914$ , GeV corresponding to the contribution 3.62%, and  $m_{\tilde{\chi}_1^0} = 1514$  GeV, corresponding to the contribution 1.66%. The maximum contribution is 6.63% which corresponds to  $m_{\tilde{\chi}_1^0} = 1114$  GeV. The majority of data points are located at  $m_{\tilde{\chi}_1^0} = 1069 - 1324$  GeV, with a contribution range 4.59 - 0.998%.

The last co-annihilation mode considered here is  $\tilde{\chi}_1^0 \tilde{\chi}_1^+ \to A_1 W^+$ , which is shown in the bottom-right panel. The data points spread between  $m_{\tilde{\chi}_1^0} = 952$  GeV, corresponding to the contribution 6.35%, and  $m_{\tilde{\chi}_1^0} = 1526$  GeV, corresponding to the contribution 3.1%. The maximum contribution is 7.1% associated with  $m_{\tilde{\chi}_1^0} = 1317$  GeV. Most data points are located at  $m_{\tilde{\chi}_1^0} = 1043 - 1338$  GeV, with a contribution range 6.82 - 0.97%.

## 4.4 $\tilde{\chi}_2^0$ and $\tilde{\chi}_1^{\pm}$ decays to the LSP

There are several decay channels producing an LSP (along with other particles), however, the decays of the chargino and the second-lightest neutralino are of special importance. Table 3, in the Appendix, lists all available branching ratios for a point in the allowed parameter space with  $\tilde{\chi}_1^0 \approx 1100$  GeV.

Fig. 6 shows that for  $\tilde{\chi}^0_2$  decays, the radiative decay  $\tilde{\chi}^0_2 \to \tilde{\chi}^0_1 \gamma$  can be significant in regions of the parameter space, where the branching ratio can reach up to  $\sim 0.8$  for a nearly degenerate mass of  $\sim 1200$  GeV for both  $\tilde{\chi}^0_2$  and  $\tilde{\chi}^1_0$ . On the other hand, an important type of decay channel for  $\tilde{\chi}^+_1$  turns out to be  $\tilde{\chi}^+_1 \to \tilde{\chi}^0_1 u \bar{d}/c\bar{s}$ , where the branching ratio lies in the range  $0.35 \leq BR(\tilde{\chi}^+_1 \to \tilde{\chi}^0_1 u \bar{d}) \leq 0.38$  for almost all of the allowed parameter space.

Other decay modes of both considered sparticles into the LSP can be important as well (see Table 3 in the Appendix). For instance, the decay  $\tilde{\chi}^0_2 \to \tilde{\chi}^0_1 Z$  can be important but in a very rare cases where it the branching ratio is equal to 1 (where difference in mass between both neutralinos is around 100 GeV), which does not represent the region where the majority of allowed points lie. Additionally, decays of  $\tilde{\chi}^0_2$  to a pair of SM  $q\bar{q}$  and and LSP can be significant,

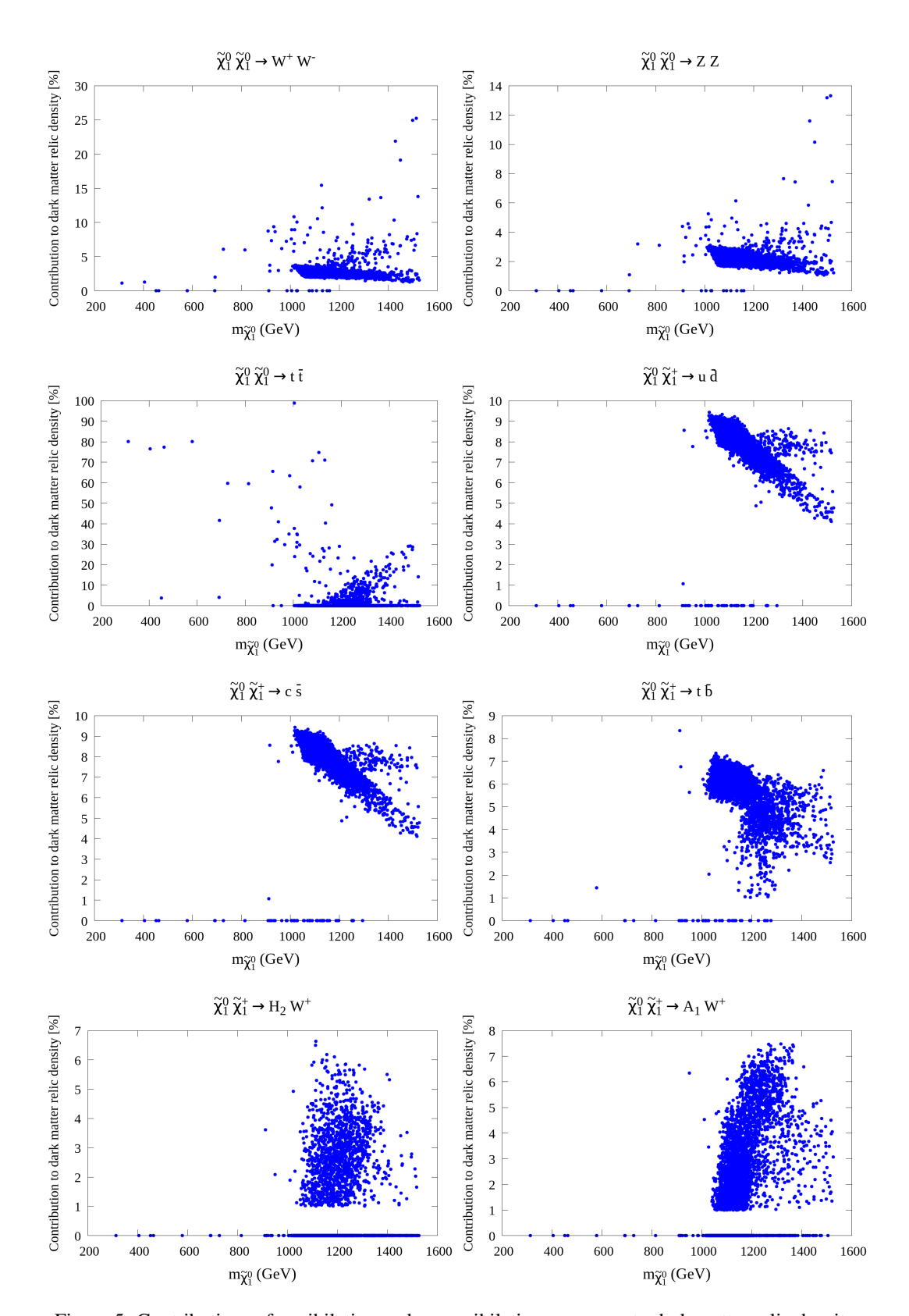


Figure 5: Contributions of annihilation and co-annihilation processes to dark matter relic density.

while weakly mediated decays of  $\tilde{\chi}_1^+$  to an LSP and a pair of  $f\bar{f}$  (where such a pair can consist of a lepton/antilepton and an antineutrino/neutrino) can also be important with branching ratio above 0.3. Moreover, it is found that for a mass range of  $1154 \le m_{\tilde{\chi}_2^0} \le 1517$  GeV, the decay channel  $\tilde{\chi}_2^0 \to \tilde{\chi}_1^0 H_1$  has a branching ratio that is close to unity  $0.94 \le BR(\tilde{\chi}_2^0 \to \tilde{\chi}_1^0 H_1) \le 1$  for a small number of successful points (where the mass difference betweenthe two neutralinos is 300 GeV minimum). The results of the branching ratios for  $\tilde{\chi}_1^+ \to \tilde{\chi}_1^0 W^+$  indicate that the branching ratio equal to 1 mostly in the range  $m_{\tilde{\chi}_1^+} = 1151 - 1513$  GeV for a limited number of successful points (where the mass difference between the chargino and the neutralino is 300 GeV minimum). The lower value  $BR(\tilde{\chi}_1^+ \to \tilde{\chi}_1^0 W^+) = 0.033$  corresponding to  $m_{\tilde{\chi}_1^+} = 849$  GeV.

Finally, in the scanned parameter space, some of the remaining decay channels of  $\tilde{\chi}^0_2$  and  $\tilde{\chi}^+_1$  into  $\tilde{\chi}^0_1$  have a range of branching ratios that reaches a maximum branching ratio value of  $0.4~(\tilde{\chi}^+_1\to\tilde{\chi}^0_1c\bar{s}), 0.15~(\tilde{\chi}^+_1\to\tilde{\chi}^0_1e^+\nu_e), 0.12~(\tilde{\chi}^+_1\to\tilde{\chi}^0_1\mu^+\nu_\mu), 0.08~(\tilde{\chi}^+_1\to\tilde{\chi}^0_1\tau^+\nu_\tau),$  and  $0.14~(\tilde{\chi}^0_2\to\tilde{\chi}^0_1c\bar{c}), 0.18~(\tilde{\chi}^0_2\to\tilde{\chi}^0_1d\bar{d}), 0.08~(\tilde{\chi}^0_2\to\tilde{\chi}^0_1\nu_{e/\mu/\tau}\bar{\nu}_{e/\mu/\tau}),$   $0.18~(\tilde{\chi}^0_2\to\tilde{\chi}^0_1s\bar{s}), 0.14~(\tilde{\chi}^0_2\to\tilde{\chi}^0_1u\bar{u}).$  Other channels are quite rare (i.e. very small branching ratio) such as  $\tilde{\chi}^0_2\to\tilde{\chi}^0_1e^+e^-, \tilde{\chi}^0_2\to\tilde{\chi}^0_1\mu^+\mu^-, \tilde{\chi}^0_2\to\tilde{\chi}^0_1\tau^+\tau^-, \tilde{\chi}^0_2\to\tilde{\chi}^0_1t\bar{t}, \tilde{\chi}^0_2\to\tilde{\chi}^0_1b\bar{b}, \tilde{\chi}^0_2\to\tilde{\chi}^0_1A_1/A_2, \tilde{\chi}^0_2\to\tilde{\chi}^0_1\tilde{\chi}^0_1H_2/H_3$  where the branching ratio reaches maximum values well below 0.1.

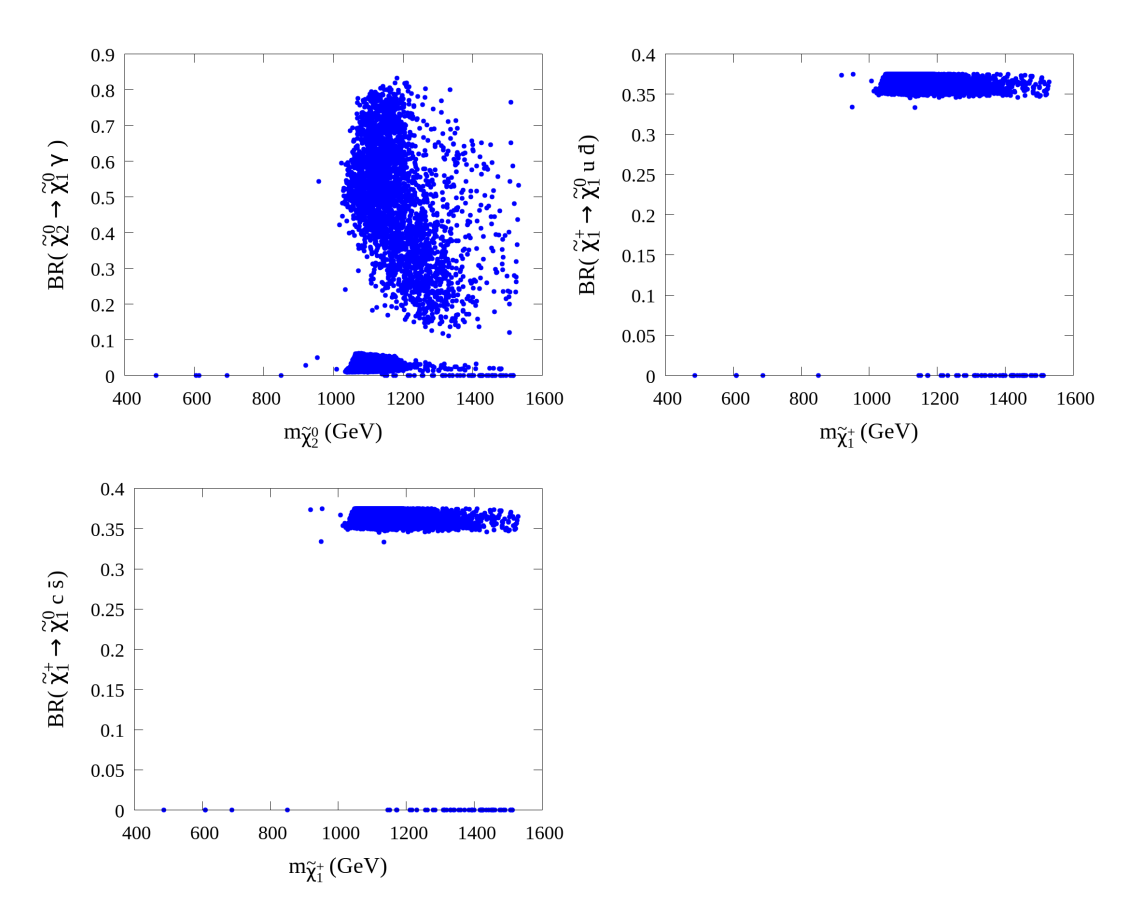


Figure 6: Branching ratios of  $\tilde{\chi}_2^0$  and  $\tilde{\chi}_1^+$  to  $\tilde{\chi}_1^0$  and other particles, where only decays with sizable Br throughout the parameter space are shown.

### 5 Discussion and conclusions

The results in the previous Section show that the NMSSM with semi-constrained GUT boundary conditions can explain current experimental observations including DM. However, the mass spectrum of the new particles, including the DM candidate (the LSP) is quite heavy. As far as the input parameters are concerned, it is observed that large values of  $m_0$  and  $m_{1/2}$  are required. As such inputs are increased, the whole SUSY spectrum increases, including the LSP dark matter. There are several reasons for this situation, the most crucial one is satisfying the bounds from direct searchers

for SUSY particles. One can still look for regions where the parameters of the model conspire to give a lighter spectrum (e.g. regions with specific relations between the gluino mass  $m_{\tilde{g}}$  or the stop mass  $m_{\tilde{t}_1}$  and  $m_{\tilde{\chi}_1^0}$ ), but we do not consider these fine-tuned cases in this paper.

Additionally, the effects of DM constraints on other NMSSM-specific parameters were considered. These parameters include  $\lambda$  and  $\kappa$ , where it is found that they can assume values between 0.1 and below 0.7, however, the majority of allowed points reside in regions where  $\lambda \lesssim 0.6$  and  $\kappa \gtrsim 0.3$ . Furthermore, the other NMSSM-specific parameters  $A_{\lambda}$  and  $A_{\kappa}$ , and for most of the allowed parameter space, are found to lies mostly in regions where  $A_{\kappa}$  is negative.

In meanwhile, it is observed that the mass content of the DM particle (the neutralino LSP) comes mostly from the Higgsino component, where in most of the parameter space it that component assumes the value 0.7, for a range of neutralino mass between 1000 GeV and 1500 GeV. The singlino component is found to be quite small (between 0 and 0.1) in the majority of the parameter space. However, this does not entirely rule-out the option of finding regions where the singlino component could be large. Indeed, it is noticed that very rare points in the scanned parameter space could achieve such large values, but such a case requires a dedicated and separate study that is beyond the scope of this paper. On the other hand, the Bino component is found to be somewhat small with values reaching up to 0.15 in most of the allowed parameter space. Again, very few points are found to have a large Bino components, and investigating such regions is also an interesting question for future research. The last component, the Wino, is found to be small throughout the allowed parameter space.

Additionally, it is observed that in most of the allowed parameter space, the annihilation of the LSP, as a mechanism for generating the required DM relic density, is not sufficient in the model. To achieve the observed value, co-annihilation must be taken into account. Indeed, it is found that co-annihilation processes with the chargino  $\tilde{\chi}_1^+$  constitute a major contributor to the dark matter relic density (given the specific allowed parameter space). Specifically, co-annihilation processes leading to  $u\bar{d}/c\bar{s}/t\bar{t}$ ,  $H_2W^+$  and  $A_1W^+$  are found to provide most of the contributions.

As for decays of heavier neutralinos and charginos to the LSP, we see that the decays of  $\tilde{\chi}^0_2$  and  $\tilde{\chi}^+_1$  are crucial given that they can be close to the mass of  $\tilde{\chi}^0_1$ . Indeed, it is observed that the radiative decay of  $\tilde{\chi}^0_2$  can be very significant accounting for about 80% of its decays, especially in regions where it has a nearly degenerate mass with  $\tilde{\chi}^0_1$ . which happens to be the region where most allowed points are found and the common mass between the two is about 1200 GeV. Other channels can be significant, albeit very rarely as we discussed in the results Section.

All in all, the NMSSM with GUT boundary conditions remains an interesting model for new physics. We showed that it can account for current observations, even though the predicted spectrum appears to be heavy. In the future, it is worth considering a dedicated study of regions where the DM particle is mostly singlino and analyze the viability of such case given the most recent stringent constraints.

### **Acknowledgements**

The authors would like to thank the Deanship of Scientific Research in King Saud University for funding and supporting this research through the initiative of DSR Graduate Students Research Support (GSR). Maien Binjonaid would like to thank Constantinos Pallis for discussions at an early stage of this work.

## **Appendix**

Here we present more details on processes contributing to the dark matter relic density via annihilation or co-annihilation (Table 2), and the branching ratios of  $\tilde{\chi}^0_2$  and  $\tilde{\chi}^\pm_1$  with  $\tilde{\chi}^0_1$  in the final state (Table 3). The results are selected for a representative point in the allowed parameter space where  $m_{\tilde{\chi}^0_1} \approx 1100$  GeV. For this point, the values of the input parameters are:  $m_0 = 3026.39$  GeV,  $m_{1/2} = 4123.10$  GeV,  $A_0 = -1742.77$  GeV,  $A_\lambda = 1809.71$  GeV,  $A_\kappa = -1742.77$  GeV,  $\lambda = 0.405937$ ,  $\kappa = 0.585409$ ,  $\tan\beta = 5.19087$  and  $\mu_{eff} = 1077.74$  GeV.

Table 2: Channels contributions to DM relic density for  $m_{\tilde{\chi}^0_1}\approx 1100$  GeV.

Channal	Contribution [07]	Channal	Contribution [07]	
Channel	Contribution $[\%]$	Channel	Contribution $[\%]$	
$\tilde{\chi}_1^0 \tilde{\chi}_1^0 \to W^+ W^-$	2.5529	$\tilde{\chi}_1^+ \tilde{\chi}_1^- \to c  \bar{c}$	2.1599	
$\tilde{\chi}_1^0 \tilde{\chi}_1^0 \to Z Z$	2.1240	$\tilde{\chi}_1^+ \tilde{\chi}_1^- \to s  \bar{s}$	1.3716	
$\tilde{\chi}_1^0 \tilde{\chi}_2^0 \to u  \bar{u}$	1.5354	$\tilde{\chi}_1^+ \tilde{\chi}_1^- \to d \bar{d}$	1.3716	
$\tilde{\chi}_1^0 \tilde{\chi}_2^0 \rightarrow d  \bar{d}$	1.9703	$\tilde{\chi}_1^+ \tilde{\chi}_1^- \to u  \bar{u}$	2.1599	
$\tilde{\chi}_1^0 \tilde{\chi}_2^0 \to c  \bar{c}$	1.5354	$\tilde{\chi}_1^+ \tilde{\chi}_1^- \rightarrow e^- e^+$	1.0600	
$\tilde{\chi}_1^{\bar{0}}\tilde{\chi}_2^{\bar{0}} \rightarrow s\bar{s}$	1.9703	$\tilde{\chi}_1^+ \tilde{\chi}_1^- \to \mu^- \mu^+$	1.0600	
$\tilde{\chi}_1^0 \tilde{\chi}_2^0 \rightarrow b \ \bar{b}$	1.9669	$\tilde{\chi}_1^+ \tilde{\chi}_1^- \to \tau^- \tau^+$	1.0589	
$\  \tilde{\chi}_1^0 \tilde{\chi}_1^+ \to u  \bar{d} $	8.2336	$\tilde{\chi}_1^+ \tilde{\chi}_1^- \to W^+ W^-$	2.4501	
$\parallel \tilde{\chi}_1^0 \tilde{\chi}_1^+ \to c  \bar{s}$	8.2335	$\tilde{\chi}_1^+ \tilde{\chi}_2^0 \to u \bar{d}$	5.2446	
$\parallel \tilde{\chi}_1^0 \tilde{\chi}_1^+ \to t  \bar{b}$	6.4884	$\tilde{\chi}_1^+ \tilde{\chi}_2^0 \to c  \bar{s}$	5.2446	
$\parallel \tilde{\chi}_1^0 \tilde{\chi}_1^+ \to \nu_e \ e^+$	2.7432	$\tilde{\chi}_1^{+}\tilde{\chi}_2^{\bar{0}} \rightarrow t \; \bar{b}$	4.1379	
$\parallel \tilde{\chi}_1^0 \tilde{\chi}_1^+ \to \nu_\mu \; \mu^+$	2.7432	$\tilde{\chi}_1^+ \tilde{\chi}_2^0 \to \nu_e \ e^+$	1.7480	
$\parallel \tilde{\chi}_1^0 \tilde{\chi}_1^+ \to \nu_\tau \ \tau^+$	2.7351	$\tilde{\chi}_1^+ \tilde{\chi}_2^0 \rightarrow \nu_\mu \; \mu^+$	1.7480	
$\parallel \tilde{\chi}_1^0 \tilde{\chi}_1^+ \to A_1 W^+$	1.7230	$\tilde{\chi}_1^+ \tilde{\chi}_2^{\bar{0}} \rightarrow \nu_{\tau} \ \tau^+$	1.7428	
$ \tilde{\chi}_1^0 \tilde{\chi}_1^+ \to \gamma W^+ $	1.2999	$\tilde{\chi}_1^+ \tilde{\chi}_2^0 \to W^+ A_1$	1.1470	
$\tilde{\chi}_1^+ \tilde{\chi}_1^- \to t  \bar{t}$	2.0057			
Sum of contribution $pprox 84\%$				

Table 3: Branching ratio to the neutralino DM at  $m_{\tilde{\chi}^0_1}\approx 1100$  GeV.

$\tilde{\chi}_1^+$ Decay Channel	Branching ratio	$ ilde{\chi}^0_2$ Decay Channel	Branching ratio
$\tilde{\chi}_1^+ \to \tilde{\chi}_1^0 \ u \ \bar{d}$	0.369013	$\tilde{\chi}_2^0 \rightarrow \tilde{\chi}_1^0 \gamma$	0.0160266
$\tilde{\chi}_1^+ \to \tilde{\chi}_1^0 \ c \ \bar{s}$	0.369013	$\tilde{\chi}_2^0 \to \tilde{\chi}_1^0 \ u \ \bar{u}$	0.127083
$\tilde{\chi}_1^+ \to \tilde{\chi}_1^0 e^+ \nu_e$	0.123004	$\tilde{\chi}_2^0 \rightarrow \tilde{\chi}_1^0 d \bar{d}$	0.165291
$\parallel \tilde{\chi}_1^+ \to \tilde{\chi}_1^0 \; \mu^+ \nu_\mu$	0.123004	$\tilde{\chi}_2^0 \to \tilde{\chi}_1^0 \ c \ \bar{c}$	0.127083
$\tilde{\chi}_1^+ \to \tilde{\chi}_1^0  \tau^+ \nu_{\tau}$	0.0159653	$\tilde{\chi}_2^0 \rightarrow \tilde{\chi}_1^0 \ s \ \bar{s}$	0.165291
		$\tilde{\chi}_2^0 \rightarrow \tilde{\chi}_1^0 e^- e^+$	0.0382097
		$\tilde{\chi}_2^0 \rightarrow \tilde{\chi}_1^0 \mu^- \mu^+$	0.0382097
		$\tilde{\chi}_2^0 \rightarrow \tilde{\chi}_1^0  \tau^-  \tau^+$	0.0176361
		$\tilde{\chi}_2^0 \rightarrow \tilde{\chi}_1^0 \nu_e \bar{\nu}_e$	0.0764173
		$\tilde{\chi}_2^0 \rightarrow \tilde{\chi}_1^0 \ \nu_\mu \ \bar{\nu}_\mu$	0.0764173
		$\tilde{\chi}_2^0 \to \tilde{\chi}_1^0  \nu_\tau  \bar{\nu}_\tau$	0.0764173
Sum of branching ratios $pprox 1$		Sum of branching ratios $\approx 0.924$	

## References

- [1] Gianfranco Bertone and Dan Hooper. History of dark matter. Rev. Mod. Phys., 90(4):045002, 2018.
- [2] Edvige Corbelli and Paolo Salucci. The Extended Rotation Curve and the Dark Matter Halo of M33. *Mon. Not. Roy. Astron. Soc.*, 311:441–447, 2000.
- [3] S.M. Faber and R.E. Jackson. Velocity dispersions and mass to light ratios for elliptical galaxies. *Astrophys. J.*, 204:668, 1976.
- [4] Steven W. Allen, August E. Evrard, and Adam B. Mantz. Cosmological Parameters from Observations of Galaxy Clusters. *Ann. Rev. Astron. Astrophys.*, 49:409–470, 2011.
- [5] Alexandre Refregier. Weak gravitational lensing by large scale structure. *Ann. Rev. Astron. Astrophys.*, 41:645–668, 2003
- [6] P.A.R. Ade et al. Planck 2015 results. XIII. Cosmological parameters. Astron. Astrophys., 594:A13, 2016.
- [7] P.A. Zyla et al. Review of Particle Physics. *PTEP*, 2020(8):083C01, 2020.
- [8] Search for direct top squark pair production in the 3-body decay mode with a final state containing one lepton, jets, and missing transverse momentum in  $\sqrt{s} = 13$ TeV pp collision data with the ATLAS detector. 5 2019.
- [9] Search for dark matter in association with an energetic photon in pp collisions at  $s_{\sqrt{=13}}$  TeV with the ATLAS detector. 6 2020.
- [10] Jeanette Miriam Lorenz. Supersymmetry and the collider Dark Matter picture. Mod. Phys. Lett. A, 34(30):1930005, 2019.
- [11] Search for chargino-neutralino pair production in final states with three leptons and missing transverse momentum in  $\sqrt{s}$  = 13 TeV p-p collisions with the ATLAS detector. 6 2020.
- [12] Georges Aad et al. Search for chargino-neutralino production with mass splittings near the electroweak scale in three-lepton final states in  $\sqrt{s}$ =13 TeV pp collisions with the ATLAS detector. *Phys. Rev. D*, 101(7):072001, 2020.
- [13] Albert M Sirunyan et al. Search for supersymmetry in proton-proton collisions at  $\sqrt{s} = 13$  TeV in events with high-momentum Z bosons and missing transverse momentum. *JHEP*, 09:149, 2020.
- [14] Gianfranco Bertone, Dan Hooper, and Joseph Silk. Particle dark matter: Evidence, candidates and constraints. *Phys. Rept.*, 405:279–390, 2005.
- [15] Ulrich Ellwanger, Cyril Hugonie, and Ana M. Teixeira. The Next-to-Minimal Supersymmetric Standard Model. *Phys. Rept.*, 496:1–77, 2010.
- [16] M. Maniatis. The Next-to-Minimal Supersymmetric extension of the Standard Model reviewed. *Int. J. Mod. Phys. A*, 25:3505–3602, 2010.
- [17] S.A. Abel, Subir Sarkar, and I.B. Whittingham. Neutralino dark matter in a class of unified theories. *Nucl. Phys. B*, 392:83–110, 1993.
- [18] A. Stephan. Dark matter constraints in the minimal and nonminimal SUSY standard model. *Phys. Rev. D*, 58:035011, 1998.
- [19] A. Stephan. Dark matter constraints on the parameter space and particle spectra in the nonminimal SUSY standard model. *Phys. Lett. B*, 411:97–106, 1997.
- [20] C. Hugonie, G. Belanger, and A. Pukhov. Dark matter in the constrained NMSSM. JCAP, 11:009, 2007.
- [21] G. Belanger, F. Boudjema, C. Hugonie, A. Pukhov, and A. Semenov. Relic density of dark matter in the NMSSM. *JCAP*, 09:001, 2005.
- [22] G. Belanger, C. Hugonie, and A. Pukhov. Precision measurements, dark matter direct detection and LHC Higgs searches in a constrained NMSSM. JCAP, 01:023, 2009.
- [23] S. Kraml, A.R. Raklev, and M.J. White. NMSSM in disguise: Discovering singlino dark matter with soft leptons at the LHC. *Phys. Lett. B*, 672:361–366, 2009.
- [24] Jin-Min Yang. Dark matter in the MSSM and its singlet extension. Mod. Phys. Lett. A, 25:976–982, 2010.
- [25] Jun-Jie Cao, Ken-ichi Hikasa, Wenyu Wang, Jin Min Yang, Ken-ichi Hikasa, Wen-Yu Wang, and Jin Min Yang. Light dark matter in NMSSM and implication on Higgs phenomenology. *Phys. Lett. B*, 703:292–297, 2011.
- [26] Ulrich Ellwanger and Cyril Hugonie. The semi-constrained NMSSM satisfying bounds from the LHC, LUX and Planck. *JHEP*, 08:046, 2014.

- [27] Kwang Sik Jeong, Yutaro Shoji, and Masahiro Yamaguchi. Higgs Mixing in the NMSSM and Light Higgsinos. *JHEP*, 11:148, 2014.
- [28] Wenyu Wang, Mengchao Zhang, and Jun Zhao. Higgs exotic decays in general NMSSM with self-interacting dark matter. Int. J. Mod. Phys. A, 33(11):1841002, 2018.
- [29] Marcin Badziak, Marek Olechowski, and Pawel Szczerbiak. Blind spots for neutralino dark matter in the NMSSM. JHEP, 03:179, 2016.
- [30] Kun Wang and Jingya Zhu. Light higgsino-dominated NLSPs in semi-constrained NMSSM. *Chin. Phys. C*, 44(6):061001, 2020.
- [31] Zhuang Li and Fei Wang. Type-II neutrino seesaw mechanism extension of NMSSM from SUSY breaking mechanisms. *Eur. Phys. J. C*, 80(8):798, 2020.
- [32] Ulrich Ellwanger and Ana M. Teixeira. NMSSM with a singlino LSP: possible challenges for searches for supersymmetry at the LHC. *JHEP*, 10:113, 2014.
- [33] C.T. Potter. Natural NMSSM with a Light Singlet Higgs and Singlino LSP. Eur. Phys. J. C, 76(1):44, 2016.
- [34] Ulrich Ellwanger and Cyril Hugonie. The higgsino–singlino sector of the NMSSM: combined constraints from dark matter and the LHC. *Eur. Phys. J. C*, 78(9):735, 2018.
- [35] Ulrich Ellwanger. Present Status and Future Tests of the Higgsino-Singlino Sector in the NMSSM. *JHEP*, 02:051, 2017.
- [36] D.G. Cerdeno, C. Hugonie, D.E. Lopez-Fogliani, C. Munoz, and A.M. Teixeira. Theoretical predictions for the direct detection of neutralino dark matter in the NMSSM. *JHEP*, 12:048, 2004.
- [37] Debottam Das and Ulrich Ellwanger. Light dark matter in the NMSSM: upper bounds on direct detection cross sections. *JHEP*, 09:085, 2010.
- [38] D. Albornoz Vasquez, G. Belanger, J. Billard, and F. Mayet. Probing neutralino dark matter in the MSSM \& the NMSSM with directional detection. *Phys. Rev. D*, 85:055023, 2012.
- [39] C. Beskidt, W. de Boer, D.I. Kazakov, and S. Wayand. Perspectives of direct Detection of supersymmetric Dark Matter in the NMSSM. *Phys. Lett. B*, 771:611–618, 2017.
- [40] Junjie Cao, Yangle He, Yusi Pan, Yuanfang Yue, Haijing Zhou, and Pengxuan Zhu. Impact of leptonic unitarity and dark matter direct detection experiments on the NMSSM with inverse seesaw mechanism. 3 2019.
- [41] Francesc Ferrer, Lawrence M. Krauss, and Stefano Profumo. Indirect detection of light neutralino dark matter in the NMSSM. *Phys. Rev. D*, 74:115007, 2006.
- [42] Tao Han, Zhen Liu, and Shufang Su. Light Neutralino Dark Matter: Direct/Indirect Detection and Collider Searches. JHEP, 08:093, 2014.
- [43] Rahool Kumar Barman, Genevieve Bélanger, Biplob Bhattacherjee, Rohini Godbole, Dipan Sengupta, and Xerxes Tata. Current bounds and future prospects of light neutralino dark matter in NMSSM, 6 2020.
- [44] Ulrich Ellwanger and Cyril Hugonie. NMSPEC: A Fortran code for the sparticle and Higgs masses in the NMSSM with GUT scale boundary conditions. *Comput. Phys. Commun.*, 177:399–407, 2007.
- [45] Ulrich Ellwanger and Cyril Hugonie. NMHDECAY 2.0: An Updated program for sparticle masses, Higgs masses, couplings and decay widths in the NMSSM. *Comput. Phys. Commun.*, 175:290–303, 2006.
- [46] Debottam Das, Ulrich Ellwanger, and Ana M. Teixeira. NMSDECAY: A Fortran Code for Supersymmetric Particle Decays in the Next-to-Minimal Supersymmetric Standard Model. *Comput. Phys. Commun.*, 183:774–779, 2012.
- [47] G. Belanger, F. Boudjema, and A. Pukhov. micrOMEGAs: a code for the calculation of Dark Matter properties in generic models of particle interaction. In *Theoretical Advanced Study Institute in Elementary Particle Physics: The Dark Secrets of the Terascale*, pages 739–790, 2013.
- [48] Florian Domingo. A New Tool for the study of the CP-violating NMSSM. JHEP, 06:052, 2015.
- [49] Georges Aad et al. Combined measurements of Higgs boson production and decay using up to  $80 \text{ fb}^{-1}$  of proton-proton collision data at  $\sqrt{s} = 13 \text{ TeV}$  collected with the ATLAS experiment. *Phys. Rev. D*, 101(1):012002, 2020.
- [50] Albert M Sirunyan et al. Combined measurements of Higgs boson couplings in proton–proton collisions at  $\sqrt{s} = 13$  TeV. Eur. Phys. J. C, 79(5):421, 2019.

- [51] Georges Aad et al. Measurements of the Higgs boson production and decay rates and constraints on its couplings from a combined ATLAS and CMS analysis of the LHC pp collision data at  $\sqrt{s} = 7$  and 8 TeV. *JHEP*, 08:045, 2016.
- [52] P. Agnes et al. Low-Mass Dark Matter Search with the DarkSide-50 Experiment. Phys. Rev. Lett., 121(8):081307, 2018.
- [53] G. Angloher et al. Results on light dark matter particles with a low-threshold CRESST-II detector. *Eur. Phys. J. C*, 76(1):25, 2016.
- [54] E. Aprile et al. Constraining the spin-dependent WIMP-nucleon cross sections with XENON1T. *Phys. Rev. Lett.*, 122(14):141301, 2019.
- [55] C. Amole et al. Dark Matter Search Results from the Complete Exposure of the PICO-60  $C_3F_8$  Bubble Chamber. *Phys. Rev. D*, 100(2):022001, 2019.